Electronic Supplementary Material (ESI) for Journal of Materials Chemistry A.

Electronic Supporting Information

Chemo-mechanical Strain Effects on Band Engineering of TiO_2 Photocatalyst for Increasing Water Splitting Activity

Yoonyoung Kim[b], Motonori Watanabe[b,d], Junko Matsuda[d], Aleksandar Staykov[d], Hajime Kusaba[a], Atsushi Takagaki[a,d], Taner Akbay[a,c], and Tatsumi Ishihara*[a,b,c,d]

[a]Department of Applied Chemistry, Faculty of Engineering, Kyushu University

[b]Graduate School of Automotive Sciences, Kyushu University

[c]Advanced Research Centre for Electric Energy Storage, Kyushu University

[d]International Institute for Carbon-Neutral Energy Research (WPI-I²CNER)

744 Motooka, Nishi-ku, Fukuoka 819-0395, Japan

Condenses are sent to:
Prof. Tatsumi Ishihara
Department of Applied Chemistry,
Faculty of Engineering, Kyushu University,
744 Motooka, Nishi-ku, Fukuoka,
819-0395, Japan.
E-mail: ishihara@cstf.kyushu-u.ac.jp
Fax;+81-92-802-2871

1. Detailed Descriptions of Methods

1) Sample preparation

Commercial TiO_2 (P-25, Degussa) was used as a starting material. A total of 1.8 g of P-25 was mixed in 200 mL of ethanol solution (ethanol:distilled water, 1:1) with heating and stirring for 60 min. An aqueous solution of H_2AuCl_4-$4H_2O$, (Kishida Chemical Co., Ltd.) was dropped slowly into the mixture and dried until evaporation. The obtained powder was heated at 623 K for 2 h to remove organic impurities. The obtained powder was sintered by the spark plasma sintering (SPS; SPS-2llLX Fuji Electronic Industrial Co., Ltd.) process, which provides a rapid temperature difference with pressure in a vacuum atmosphere for sintering. A graphite die (10 mm diameter) was filled with 0.5 g of the obtained powder and a disc was uniaxially pressed by using graphitic carbon punch at 60 MPa.

The prepared sample was sintered at 873 K for 5 min. The obtained disc was then ground to a powder by ball-milling to increase the surface area of the photocatalyst. The average surface area and particle size of the obtained TiO_2 were 14 m^2/g and 94 nm, respectively. Au loading on P-25 TiO_2 was also performed by a conventional impregnation method using an aqueous solution of H_2AuCl_4-$4H_2O$ (Kishida Chemical Co., Ltd.).

2) Photocatalytic activity

Fifty milligrams of Au-TiO_2 was used to measure photocatalytic water splitting under irradiation with a 300 W Xe lamp in an Ar atmosphere. Thirty milliliters of 10 vol% methanol solution and 0.1 M $AgNO_3$ solution were used as sacrificial reagents for H_2 and O_2 formation, respectively. Generated gases were analyzed using on-line gas chromatography (GC; GC-8A Shimadzu, MS-5A column) with a thermal conductivity detector (TCD).

3) Characterization

The phase and crystal structures were analyzed using X-ray diffraction (XRD; RINT 2500, Rigaku Co.) with Cu Kα radiation (40 kV, 80 mA). The scan speed was 5°/min in the 2θ range of 10° to 80°. For narrow scan mode, the scan angle and speed were 20-30° and 0.3°/min respectively. The lattice parameters of Au-TiO_2 were refined using the Rietveld method with the Rietan software package (PDXL 2.4, Rigaku). Oxidation states of Au and Ti were analyzed by using X-ray photoelectron spectroscopy (XPS; Kratos Ultra, Shimadzu). The binding energy of each peak was normalized with respect to the C 1s peak at 285 eV.

The lattice strain and the crystal structure were also analyzed using Raman spectroscopy (Renishaw, type InVia Qontor) with Nd:YAG_laser (532 nm, 150 mW) as a light source. TiO_2 and Au-TiO_2 were analyzed in the wavelength range from 1050 to 100 cm^{-1}. Electron spin resonance (ESR) spectroscopy measurements were conducted with an ESR spectrometer (EMS 8/2.7s, Bruker Biospin). The sample powder was loaded into a quartz glass tube. All ESR spectra were measured at room temperature. UV-vis spectroscopy (U3310, Hitachi) was conducted to analyze the change in the bandgap. The morphology and composition of Au-TiO_2 were observed using transmission electron microscopy (TEM; JEM-ARM 200, JEOL). Electron energy loss spectroscopy (EELS; Gatan Co. Ltd.) measurements were also performed to determine the electronic states of the elements. Photoluminescence (PL) spectroscopy and transient photoluminescence were measured for analysis of the charge transfer efficiency using a Hitachi F-7000 fluorescence spectrophotometer and a Horiba Fluoro Cube spectrophotometer, respectively.

4) Computational method

First principles calculations in the density functional theory (DFT) formalism were conducted using the Vienna *Ab initio* Simulation Package (VASP)[18,19,20] with the projector-augmented wave (PAW)[21] method to describe the interactions between core and valence electrons. Spin-polarization calculations were performed using the hybrid functional approach developed by Heyd, Scuseria, and Ernzerhof (HSE06)[22] based on a screened coulombic potential for the exchange interaction. In this approach, exactly 25% Hartree-Fock (HF) exchange is mixed with the Perdew, Burke, and Ernzerhof (PBE)[23,24] functional with a screening term of 0.2 $Å^{-1}$. The semi-core states of Ti ($3p^6$, $4s^2$, and $3d^2$), and valence states of O ($2s^2$ and $2p^4$) were employed in all sets of geometry optimization, electronic structure, and density of states (DOS) calculations for both anatase ($I4_1/amd$) and rutile ($P4_2/mnm$) phases of TiO_2. Gamma-centered k-point meshes with 4×4×2 and 4×4×6 divisions were used for sampling the first Brillouin zones of the anatase and rutile crystal structures, respectively. The kinetic energy cutoff point for the plane-wave basis sets was selected as 520 eV. The convergence criteria for electronic self-consistency and ionic relaxation calculations were set as 10^{-5} eV and 0.01 eV/Å, respectively. The purpose of the first principles calculations was to identify the lattice strain dependence of the bandgap for each TiO_2 phase; therefore, the crystal structures were subjected to various degrees of compressive and tensile strain (from –2% to +2%) prior to ions-only geometry optimization calculations.

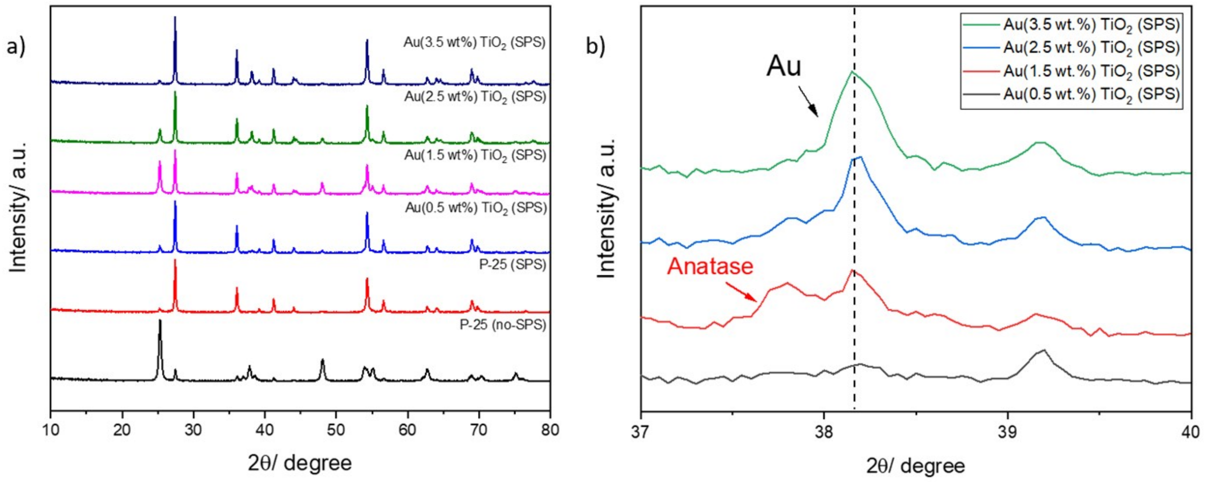

Fig. S1 (a) Wide angle XRD patterns for TiO_2 with dispersed Au after SPS treatment and (b) XRD peaks for Au in TiO_2 with various Au content.

Wide angle XRD patterns are shown in Fig. S1; peaks from both anatase and rutile TiO_2 were observed. No peaks from secondary phases were observed. Fig. S1(b) shows a magnified XRD pattern at the position of the strongest Au peak from the database, and it was confirmed that the intensity of the XRD peak assigned to Au was strengthened with an increase in the amount of Au. Therefore, it was confirmed that no reaction between TiO_2 and Au occurred. Weak diffraction peaks from metallic Au were observed, which indicated the Au dispersed in TiO_2 was metallic.

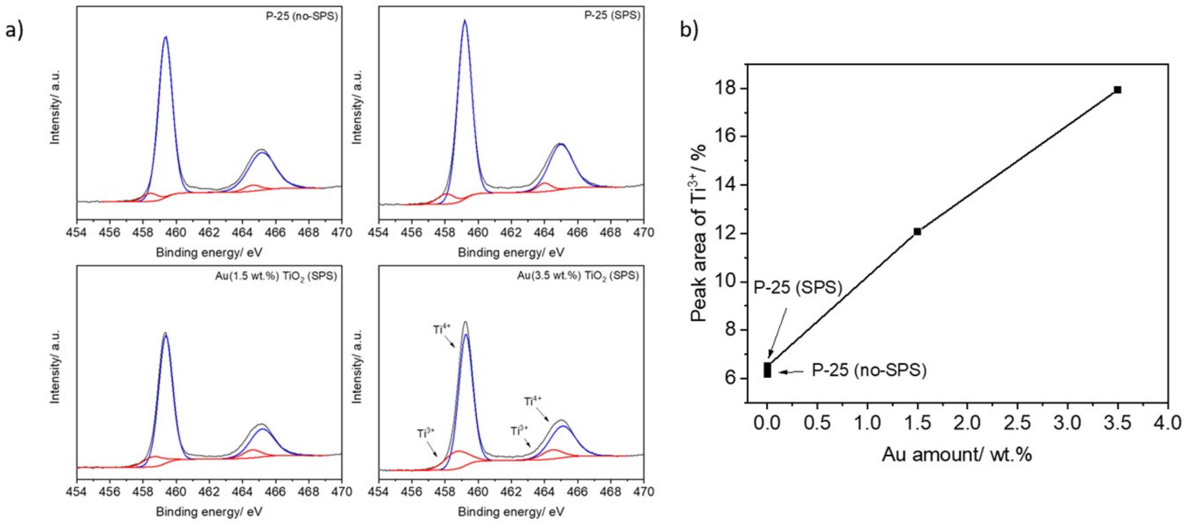

Fig. S2 (a) Peak separation of XPS Ti 2p peak for Au-dispersed TiO$_2$ after SPS treatment. (b) Estimated relative amount of Ti^{3+} as a function of the amount of dispersed Au.

Fig. S2(a) and (b) show the peak separation of the XPS Ti 2p peak and the estimated Ti^{3+} peak area as a function of the amount of Au, respectively. Ti^{3+} was observed after SPS treatment and the peak area was increased with the amount of dispersed Au. Therefore, the formation of Ti^{3+} and oxygen vacancies by charge compensation was increased by SPS treatment and more significantly by the tensile strain induced.

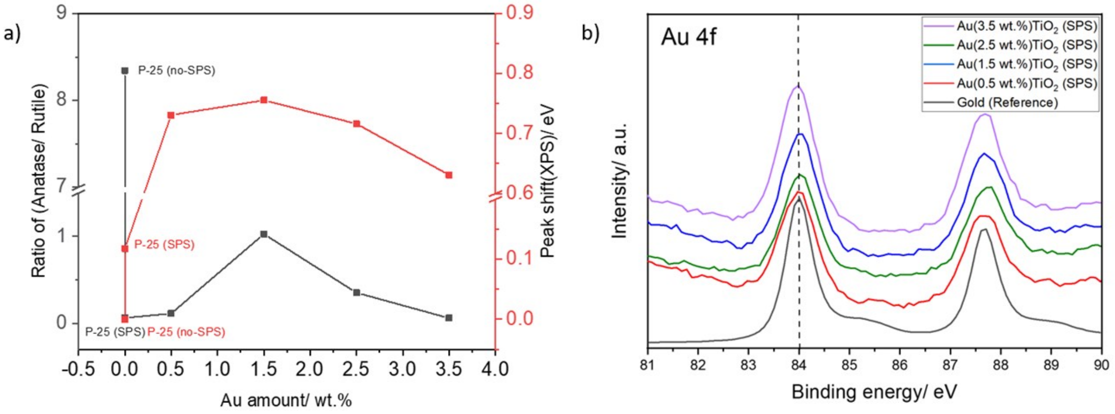

Fig. S3(a) Anatase to rutile ratio as a function of the Au content. (b) XPS Au 4f spectra for TiO_2 with various Au content.

Fig. S3(a) shows the anatase/rutile ratio as a function of the amount of Au. After SPS treatment, the anatase/rutile ratio was close to 0, which indicated that all TiO_2 were changed to the rutile phase. On the other hand, as the amount of Au increased, the anatase/rutile ratio was increased and became the largest at 1.5 wt% Au. Therefore, Au dispersion is effective for stabilization of the anatase phase. This is the first time observation on stabilizing the anatase phase by strain effects.

Fig. S3(b) shows XPS peaks of Au 4f orbitals, where the binding energy (BE) indicates the Au 4f level is metallic; therefore, the chemical state of dispersed Au is metallic. The BE value was not significantly changed with the amount of Au.

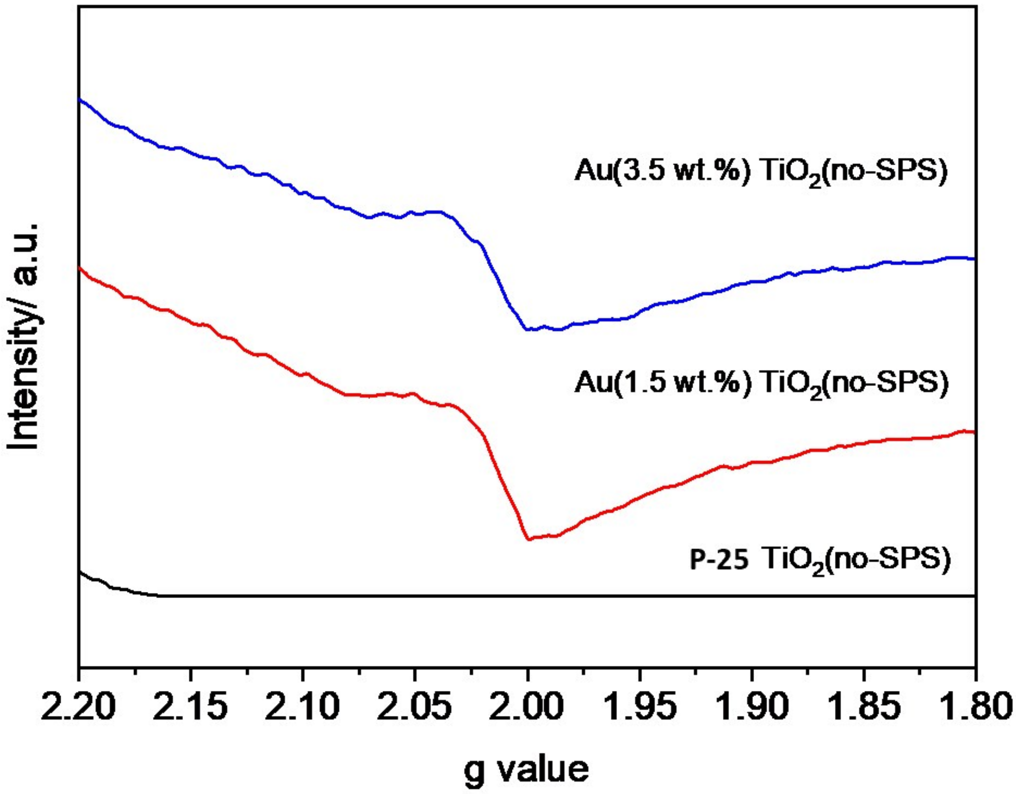

Fig. S4. ESR spectra for TiO_2 with various Au content.

Fig. S4 shows ESR spectra for Au-loaded TiO_2. After Au loading, a weak ESR signal was observed at g=2.00, which could be assigned to an oxygen radical species that was also observed for Au-dispersed TiO_2 after SPS treatment. However, the lack of an ESR signal at around g=1.94 indicated that Ti^{3+} was not formed by loading with Au. Therefore, the formation of Ti^{3+} and oxygen vacancies could be assigned to strain effects caused by the dispersion of Au as shown in Fig.4.

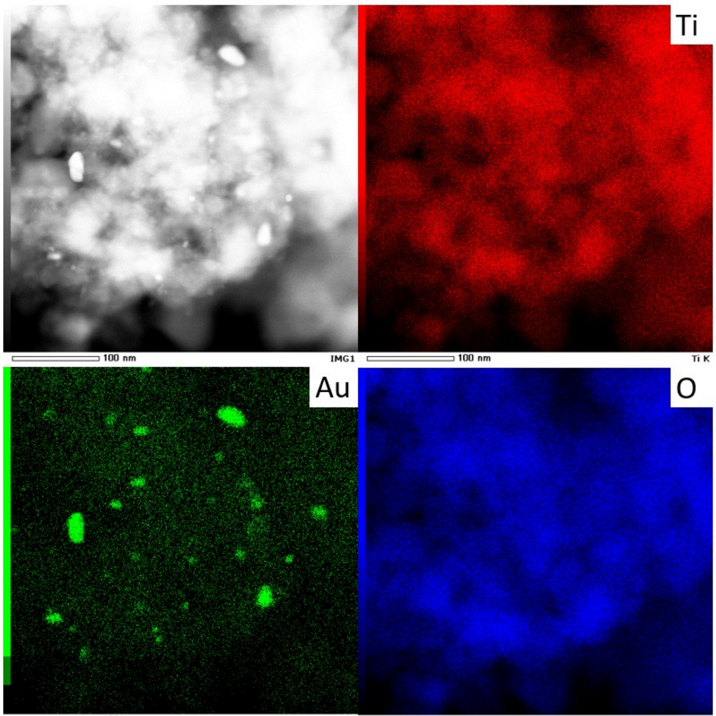

Fig. S5 Dark field STEM image of 1.5 wt% Au-dispersed TiO_2 and EDX maps for Ti, O, and Au.

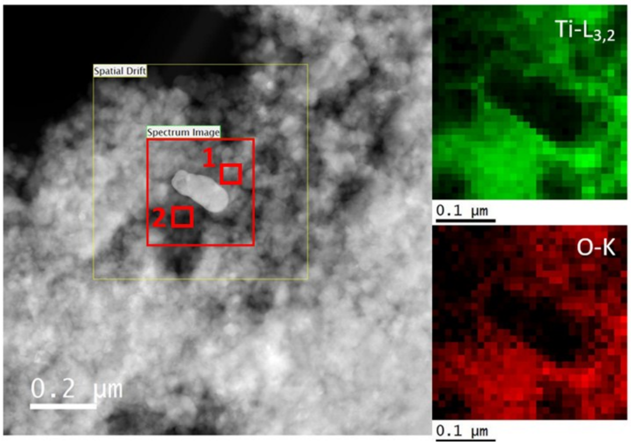

Fig. S6 Dark field STEM image of 1.5 wt% Au-dispersed TiO_2 and high magnification EDX maps for Ti and O.

Fig. S5 and S6 show STEM image of 1.5 wt% Au-dispersed TiO_2 and EDX maps for Ti, O, and Au. A high contrast image between Ti, O and Au was observed, which suggests that no reaction between Au and TiO_2 occurred, and Au is in the metallic state. The metallic state of Au was also supported by XPS analysis, as shown in Fig. S3(b).

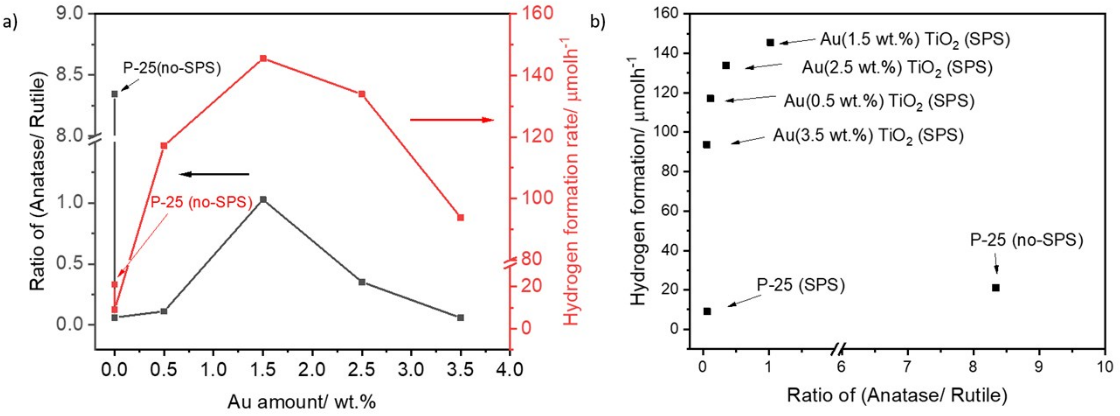

Fig. S7(a) Anatase to rutile ratio and (b) rate of H_2 formation as a function of the amount of dispersed Au.

Fig. S7 shows the anatase to rutile ratio and H_2 formation rate as a function of the amount of dispersed Au. The H_2 formation rate was significantly increased with the Au content and the highest H_2 formation rate was achieved at 1.5 wt% Au, after which it decreased with further increase in the Au content. The anatase phase of TiO_2 is known to be active for photocatalytic water splitting; Fig. S7(b) shows the H_2 formation rate as a function of the anatase to rutile ratio. There was no clear relationship between the H_2 formation rate and the relative amount of anatase, which suggests that the increase in the photocatalytic activity was not due to the large anatase content but to the unique structure of the catalyst, i.e., the anatase phase is surrounded by the rutile phase, which contains Ti^{3+} and oxygen vacancies due to the tensile strain.

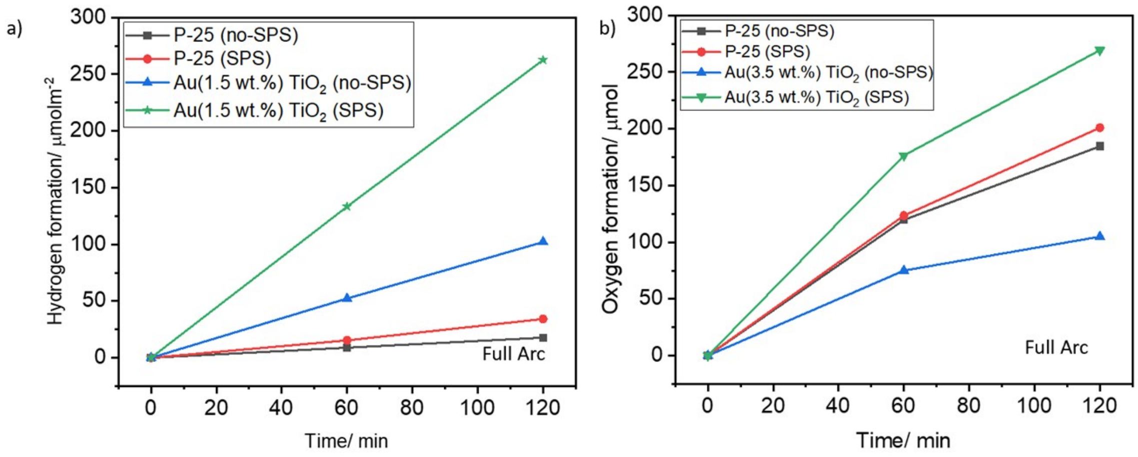

Fig. S8. (a) Rate of H_2 formation on Au-loaded TiO_2 (Au impregnated on SPS, P-25) without SPS treatment and Au-dispersed TiO_2 with SPS treatment. Methanol was used as a sacrificial reagent. (b) Rate of O_2 formation on P-25 TiO_2, Au-loaded P-25 TiO_2 and 3.5 wt% Au-dispersed TiO_2 with and without SPS treatment as a function of the reaction time. $AgNO_3$ was used as a sacrificial reagent.

Fig. S8(a) compares the rate of H_2 formation for Au-loaded P-25 TiO_2 and Au-dispersed TiO_2 with and without SPS treatment. The rate of H_2 formation was significantly increased by loading of Au on P-25 TiO_2 without SPS treatment, which indicates that Au acts as a co-catalyst and increases the activity for water splitting.[39-41] However, compared with the H_2 formation rate over Au-loaded TiO_2 (non SPS), that over Au-dispersed TiO_2 with SPS treatment was higher. Some Au particles are not exposed to the surface; therefore, it is considered that the activity per Au surface area exposed was much higher photocatalytic water splitting activity on Au-dispersed TiO_2 with SPS treatment than that of Au-loaded P-25 TiO_2 with SPS treatment. It is also noted that plasmon effects are not responsible for the increased photocatalytic activity, because the Au-dispersed TiO_2 catalyst shows a much higher H_2 formation rate than that over the Au-loaded P-25 TiO_2. The reason is because comparative plasmon effects would be expected more significant for Au-dispersed TiO_2 catalysts since the particle size of Au is much finer on Au loaded P-25 TiO_2.

Fig. S8(b) shows the rate of O_2 formation over P-25 TiO_2, Au-loaded P-25 TiO_2 and 3.5 wt% Au-dispersed TiO_2 as a function of the reaction time. A much higher rate of O_2 formation was observed over Au-dispersed TiO_2 (SPS), which indicates that the tensile strain is also effective to increase the rate of O_2 formation.

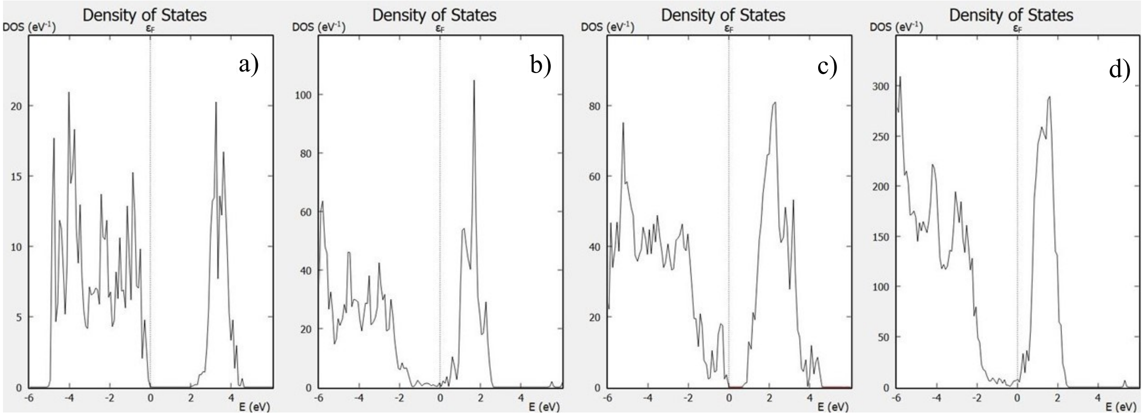

Fig. S9. DOS spectra of the anatase phase for the following junctions: A: pure anatase; B: gold 111 / anatase 001 junction; C: anatase 001 / rutile 110 junction; D: gold 111 / anatase 001 / rutile 110 junction.

We compare the density of states (DOS) spectra of anatase-only phase for four structures: A: pure anatase; B: gold 111 / anatase 001 junction; C: anatase 001 / rutile 110 junction; D: gold 111 / anatase 001 / rutile 110 junction. In this way, we can elucidate the effects of the gold / TiO_2 and anatase / rutile interfaces on the anatase electronic properties. We should not that with our choice of Hubbard DFT+U parameter the anatase bandgap is systematically underestimated. The correct bandgap for anatase is obtained with U_{Ti} = 7.5 eV[25] however the redox properties of Ti are better captured with U_{Ti} = 3.0 eV[25] which is adopted in our study. Fig. S9(b) shows that the gold / TiO_2 interface leads to levels within the bandgap, both, above the anatase valence band and below the anatase conduction band. As a result of those states the Fermi level of anatase is shifted to higher energies. Fig. S9(c) shows that the anatase 001 / rutile 110 interface leads to levels in the anatase bandgap above the valence band, thus, shifting the valence band edge to higher energies. This effect can be attributed to oxide vacancies migration into the anatase phase. As a result of the anatase 001 / rutile 110 interface the band gap has been systematically reduced to half of the energy of the bandgap of pure anatase phase.

Table S1. Fitting results of transient PL decay curves

Sample	τ_1(ns)	τ_2(ns)	τ_3(ns)
TiO_2(no-SPS)	1.42	5.47	22.80
TiO_2(SPS)	1.47	6.15	23.10
Au(1.5 wt.%)TiO_2(no-SPS)	1.37	5.62	23.17
Au(1.5 wt.%)TiO_2(SPS)	0.93	3.74	17.79

Fit equation:

$$I(t)=\sum_{i}^{n}\alpha_i \exp(-t/\tau_i)$$

Table S1 summarizes the fitting parameters for the PL decay curves of Au-dispersed TiO_2. Au-loading or SPS treatment without Au showed no change in the PL decay parameters; however, the PL decay parameters were significantly decreased by Au dispersion followed by SPS sintering. Therefore, the introduction of tensile strain is effective for the separation of the photoexcited charge.

REFERENCES:

21 G. Kresse and J. Hafner, Phys. Rev. B, 1993, **47**, 558–561.

22 G. Kresse and J. Hafner, Phys. Rev. B, 1994, **49**, 14251.

23 G. Kresse and J. Furthmiiller, J. / Am. Water Work. Assoc., 2004, **6**, 15–50.

24 G. Kresse, J. Furthmüller, Y. J. Li, Y. J. Chen, J. C. Walmsley, R. H. Mathinsen, S. Dumoulin, H. J. Roven, S. Yip, T. Supervisor and S. Chen, Phys. Rev. B, 2000, **62**, 11169–11186.

25 F. Han, Probl. Solid State Phys. with Solut., 2011, **50**, 391–396.

26 A. V. Krukau, O. A. Vydrov, A. F. Izmaylov and G. E. Scuseria, J. Chem. Phys., 2006, **125**, 0–5.

27 J. P. Perdew, K. Burke and M. Ernzerhof, Phys. Rev. Lett., 1996, **77**, 3865–3868.

28 Z. Hu and H. Metiu, J. Phys. Chem. C, 2011, **115**, 5841–5845.